RESEARCH ARTICLE

[1] Institute of High Energy Physics, Chinese Academy of Sciences, Beijing 100049, China; [2] Spallation Neutron Source Science Center, Dongguan 523803, China; [3] Beijing National Laboratory for Condensed Matter Physics, Institute of Physics, Chinese Academy of Sciences, Beijing 100080, China; [4] Department of Physics & Astronomy and Stewart Blusson Quantum Matter Institute, University of British Columbia, Vancouver V6T 1Z4, Canada; [5] State Key Laboratory of Advanced Welding and Joining Harbin Institute of Technology, Harbin 150001, China; [6] School of Advanced Energy, Sun Yat-Sen University, Shenzhen 518107, China; [7] J-PARC Center, Japan Atomic Energy Agency, Tokai, Ibaraki 319-1195, Japan; [8] Shenzhen Key Laboratory of Thermoelectric Materials, Department of Physics, Southern University of Science and Technology, Shenzhen 518055, China; [9] Guangdong Provincial Key Laboratory of Advanced Thermoelectric Materials and Device Physics, Southern University of Science and Technology, Shenzhen 518055, China; [10] Advanced Research Institute of Multidisciplinary Sciences, Qufu Normal University, Qufu 273165, China; [11] Department of Physics and Astronomy, University of Missouri, Columbia, 65211, USA; [12] Key Laboratory of Artificial Structures and Quantum Control, School of Physics and Astronomy, Shanghai Jiao Tong University, Shanghai 200240, China and [13] State Key Laboratory of Structural Chemistry, Fujian Institute of Research on the Structure of Matter, Chinese Academy of Sciences, Fuzhou 350002, China

PHYSICS

Strong low-energy rattling modes enabled liquid-like ultralow thermal conductivity in a well-ordered solid

Peng-Fei Liu [ID][1,2,†], Xiyang Li[3,4,†], Jingyu Li[1,2], Jianbo Zhu[5], Zhen Tong[6], Maiko Kofu[7], Masami Nirei[7], Juping Xu[1,2], Wen Yin[1,2], Fangwei Wang[2,3], Tianjiao Liang[1,2], Lin Xie[8,9], Yongsheng Zhang[10], David J. Singh[11], Jie Ma [ID][12], Hua Lin[13,*], Junrong Zhang[1,2,*], Jiaqing He [ID][8,9,*] and Bao-Tian Wang [ID][1,2,*]

ABSTRACT

Crystalline solids exhibiting inherently low lattice thermal conductivity (κ_L) are of great importance in applications such as thermoelectrics and thermal barrier coatings. However, κ_L cannot be arbitrarily low and is limited by the minimum thermal conductivity related to phonon dispersions. In this work, we report the liquid-like thermal transport in a well-ordered crystalline $CsAg_5Te_3$, which exhibits an extremely low κ_L value of $\sim$0.18 $Wm^{-1}K^{-1}$. On the basis of first-principles calculations and inelastic neutron scattering measurements, we find that there are lots of low-lying optical phonon modes at $\sim$3.1 meV hosting the avoided-crossing behavior with acoustic phonons. These strongly localized modes are accompanied by weakly bound rattling Ag atoms with thermally induced large amplitudes of vibrations. Using the two-channel model, we demonstrate that coupling of the particle-like phonon modes and the heat-carrying wave-like phonons is essential for understanding the low κ_L, which is heavily deviated from the $1/T$ temperature dependence of the standard Peierls theory. In addition, our analysis indicates that the soft structural framework with liquid-like motions of the fluctuating Ag atoms is the underlying cause that leads to the suppression of the heat conduction in $CsAg_5Te_3$. These factors synergistically account for the ultralow κ_L value. Our results demonstrate that the liquid-like heat transfer could indeed exist in a well-ordered crystal.

Keywords: thermal conductivity, thermoelectric, phonon dynamic, inelastic neutron scattering

Corresponding authors.
E-mails: linhua@fjirsm.ac.cn;
jrzhang@ihep.ac.cn;
hejq@sustech.edu.cn;
wangbt@ihep.ac.cn

[†] Equally contributed to this work.

INTRODUCTION

The exploration of solid materials with ultralow lattice thermal conductivity (κ_L) is of great interest due to their important applications as thermal insulators [1], thermal barrier coatings [2] and thermoelectric materials [3,4]. Strategies for suppressing phonon propagation and reducing thermal conductivity include the introduction of multidimensional defects into the material matrix [5], atomic ordering [6], high-entropy engineering [7] and others [8]. However, many strategies require the property of low thermal conductivity. As a result, screening low κ_L materials has become an important step [9–11]. In insulators, the thermal conductivity can be controlled mainly by the lattice component, κ_L, while, in doped semiconductors used as

thermoelectrics, both the lattice and the electronic components contribute to thermal conductivity. Controlling the lattice portion is crucial for high thermoelectric performance, especially in low- and medium-temperature zones.

In crystalline materials, both the transverse and longitudinal acoustic phonons contribute to the κ_L [12,13]. In liquids, if we do not consider the convection, the thermal transport is mainly governed through longitudinal vibrations [14]. Therefore, solids are usually more conductive than nonconvective liquids. Liquids can also exhibit a lower heat capacity than solids due to the absence of stable transverse modes, reducing their thermal conductivity. As a result, solids that have liquid-like vibrational spectra will exhibit low thermal conductivity,

due to both reductions in specific heat and propagating transverse modes [15–17]. This has guided the design and experimental demonstration of ultralow-κ_L crystalline compounds [18], such as Cu_2Se [19,20], $AgCrSe_2$ [21], Cu_4TiSe_4 [22], Cu_7PSe_6 [23], Ag_8SnSe_6 [24,25] and Ag_9GaSe_6 [26]. Some of these crystals have liquid-like mobile ions, which significantly reduce the thermal conductivity. Generally, the so-called phonon-liquid electron-crystal materials have large unit cells, with highly disordered atoms and complex structures [8,10,27]. These materials commonly exhibit low κ_L. Although many ultralow-κ_L crystalline compounds have been explored, the liquid-like κ_L in well-ordered crystals is rarely explored both in theoretical predictions and experiments.

$CsAg_5Te_3$ [28], a well-ordered single-phase material, was recently reported to achieve a high figure of merit (ZT) of about 1.5 at 727 K, without any extrinsic doping [29], making it a promising mid-temperature thermoelectric single-phase bulk material [30,31]. This is especially important considering that the optimization of the carrier concentration could yield an even higher ZT. The key feature of $CsAg_5Te_3$ was found to be its exceedingly low κ_L of $\sim$0.18 W m^{-1} K^{-1} at 300 K [29]. This value is even lower than those of the phonon-liquid electron–crystal materials [13,18] and is within a factor of only seven times the thermal conductivity of air ($\sim$0.025 W m^{-1} K^{-1} at 300 K). Meanwhile, with increasing temperature, the κ_L of $CsAg_5Te_3$ shows nearly temperature-independent behavior, which is different from the expectations of a semiconductor with propagating phonons governed by the Peierls–Boltzmann equation [31–33].

In this work, we used inelastic neutron scattering (INS) and first-principles calculations, supplemented with transport measurements, to elucidate the relationship between the phonon picture of atomic vibrations and the extremely low-κ_L behavior of a well-ordered crystalline $CsAg_5Te_3$. Our INS experiments show that there exist strongly localized low-lying phonon bands at $\sim$3.1 meV. When combined with calculations, we found that they are mainly dominated by the rattling Ag atoms with the avoided-crossing feature of acoustic and optical phonon branches. These Ag atoms have liquid-like motions as melted sublattices in $CsAg_5Te_3$, which is connected with the ultralow κ_L. Based on the two-channel thermal conductivity calculations, we corroborated the predominant role of the wave-like phonons, as well as the important role of the coupling between the coherent wave-like modes and the localized particle-like modes. Our study provided an overall understanding of the liquid-like heat transport in a well-ordered crystal, which would facilitate the designing of low-κ_L materials.

RESULTS

Experimental and theoretical phonons

$CsAg_5Te_3$ crystallizes in the tetragonal space group, $P4_2/mnm$, and its Zintl-type structure has two open tunnels and two infinite parallel $[Ag_5Te_3]^{-1}$ chains along the c-axis [29] (see Fig. S1). In the chains, the Ag atoms are tetrahedrally or triangularly coordinated with the Te atoms to form a structural framework with weak chemical bonds [34]. The large-radius Cs^+ ions (1.74 Å) have a large atomic mass fill in the tunnels at the center (0.5, 0.5, 0.5) and the origin (0, 0, 0) of the unit cell, stabilizing the structure. The pure polycrystalline sample is verified by the neutron diffraction data at 300 K, which are analysed by using the method of Rietveld refinement with the two strongest peaks of (550) and (552) marked in Fig. S2.

We first plot in Fig. 1a and Fig. S3 the dynamic structure factor S($\mathbf{Q}$, E) at different temperatures with INS on the powder samples to analyse the lattice dynamics. As shown on the left side of Fig. 1a, our INS measurements of the orientation averaged S($\mathbf{Q}$, E) at 295 K reveal a striking mushroom-like scattering pattern, near the quasi-Brillouin-zone center at $\mathbf{Q} = 2.7$ Å^{-1} and around a phonon frequency of 3.1 meV. The computed S($\mathbf{Q}$, E) at 300 K based on first-principles methods is plotted on the right side of Fig. 1a, which shows excellent agreement with the INS data in both phonon energies and intensities. To rationally understand these mushroom-like low-energy modes, we calculate the S($\mathbf{Q}$, E)-weighted phonon dispersion in the first Brillouin zone along the high-symmetry lines in Fig. 1b and Fig. S4 at 300 K using the same parameters as shown in Fig. 1a. This could serve as a powerful method to probe the single-crystal S($\mathbf{Q}$, E) based on the polycrystalline samples. As shown in Fig. 1b and Fig. S4, only the longitudinal vibrations of the acoustic phonons propagate along Γ–X–M–Γ–Z and are cut off starting at $\sim$2 meV by numerous optical branches and typically accompanied by the rattling modes [35]. One low-energy optical mode is observed along X–M. In the case of the other directions, there are only a few optical modes evident at <10 meV, with one flat mode at 15 meV along Z–R–A–Z. More specifically, most modes do not appear visibly in the spectrum while the longitudinal acoustic vibrations survive. Usually, phonon dispersions should be measured by INS using different regions of reciprocal space for a single crystal [36]. The simulations only in the first Brillouin zone cannot
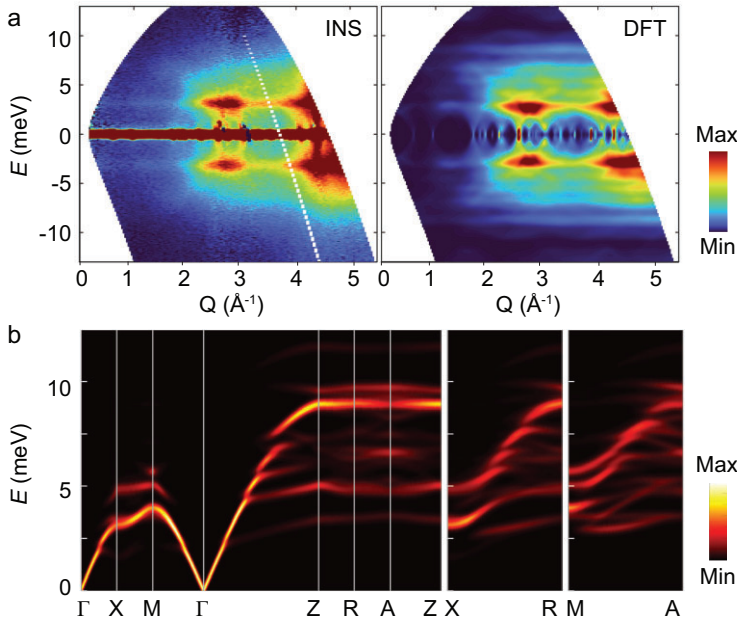
Figure 1. Experimental and calculated phonons of CsAg$_5$Te$_3$. (a) The contour plots of the dynamic structure factor $S(\mathbf{Q}, E)$ obtained by INS with an incident neutron energy of $E_i = 15.15$ meV at 295 K from the AMATERAS measurements (left) and the corresponding powder-averaged coherent $S(\mathbf{Q}, E)$ at 300 K generated by the temperature-dependent force constants from MD via first-principles calculations (right). These results clearly show that there were low-lying phonon modes at ∼3.1 meV. (b) Corresponding $S(\mathbf{Q}, E)$ weighted phonon dispersion relationship in the first Brillouin zone at 300 K calculated by Euphonic. To facilitate comparison between experiments and theory, we have normalized $S(\mathbf{Q}, E)$ in these figures.

capture the whole picture of the phonons. Since the high-resolution neutron diffraction data show that there are two strong peaks at (550) and (552) (see Fig. S2), we calculate the $S(\mathbf{Q}, E)$-weighted spectra for the Brillouin zones centered at the (550) and (552) zones and present them in Fig. S5. It clearly shows that all the acoustic phonons participate in the propagation. This is different from the superionic conductors [20], in which the structurally dynamic disorder damages the transverse acoustic phonons. Most notably, the powder INS data presented here provide an average density of states for all directions and regions of reciprocal space, while Fig. 1b and Fig. S2 only correspond to the two zones along specific directions. Beyond that, our theoretical and experimental results indeed demonstrate the existence of low-lying phonon modes. From first-principles calculations, we see that there exist the avoided crossings of optical–acoustic branches with the emerging concerted rattling modes [29] in Fig. S6. These in turn modulate the group velocities and scattering process, and also suppress the κ_L. In addition, we have calculated the participation ratio (PR) and spatial distribution of the phonon modes in Fig. S7. Clearly, the PR values in Fig. S7 of

the low-lying optical modes at ∼3.1 meV are close to ∼0.2, which means that these modes are likely localized [37]. The spatial distribution shows that the localized phonons with energy of <4 meV are mostly in the Ag atoms. The existence of abundant localized phonons often occurs in non-crystalline materials, quasicrystals and nanostructured materials, which would cause a transition from propagative to diffusive-like energy transport [37,38]. For our system, it brings about the abnormal ultralow two-channel heat transport mechanism in CsAg$_5$Te$_3$, as discussed below.

The temperature-dependent behavior of the low-energy phonons is analysed by integrating the $S(\mathbf{Q}, E)$ data over $1.5 \leq \mathbf{Q} \leq 3.5$ Å^{-1}, as shown in Fig. 2a. At 8 and 100 K, we observe one prominent peak, as marked by the stars, as well as several less intense peaks. Upon heating from 295 to 655 K, there is only one intense peak in the indicated region. This big peak is far away from the intense elastic line and corresponds to the low-lying phonon modes at around $\mathbf{Q} = 2.7$ Å^{-1}, as shown in Fig. 1 and Fig. S4. The scattering is further analysed in real space by Fourier-transforming the static structure factor into the pair distribution functions (PDFs). Figure 2b shows the PDFs for the pair distances from 2.5 to 11.5 Å at selected temperatures. Figs S8 and S9 show the first peak located at ∼2.83 Å. The superposition of the nearest neighboring Ag–Te and Ag–Ag bonds, which correspond to the structural tunnels in the crystal structure without local structural distortions, induces the absence of the shoulder peak at ∼2.83 Å [39].

When the temperature is increased, the amplitude of the first peak in Fig. 2b is monotonically decreased, while other peaks of >3.5 Å are significantly affected and smoothed out. This clearly indicates that the structural framework is preserved well upon heating but exhibits substantial atomic motions. The long-distance pairs gradually lose their correlation upon heating. This fact is further confirmed by our simulated trajectories of the atoms in the x–y plane at 300, 500 and 700 K by the molecular dynamics (MD) simulations, as presented in Figs S10 and S11. In Fig. S12, the self-part of the van Hove correlation function $G_s(r, t)$ calculated from the MD simulations depicts the probability of atoms diffusing away from the initial positions by a distance r after a period t. As time goes on, the $G_s(r, t)$ fluctuate at a fixed value for all atoms. There are no jump diffusions for all atoms in CsAg$_5$Te$_3$. Meanwhile, our calculated Lindemann parameter, $\delta = ADP^{1/2}/R_{NN}$ (where R_{NN} is the nearest neighbor distance and ADP is the atom displacement parameters), is 0.0415, 0.0494/0.050 and 0.061/0.076/0.079 for Cs, Te and Ag atoms, respectively. Clearly, the values of Ag
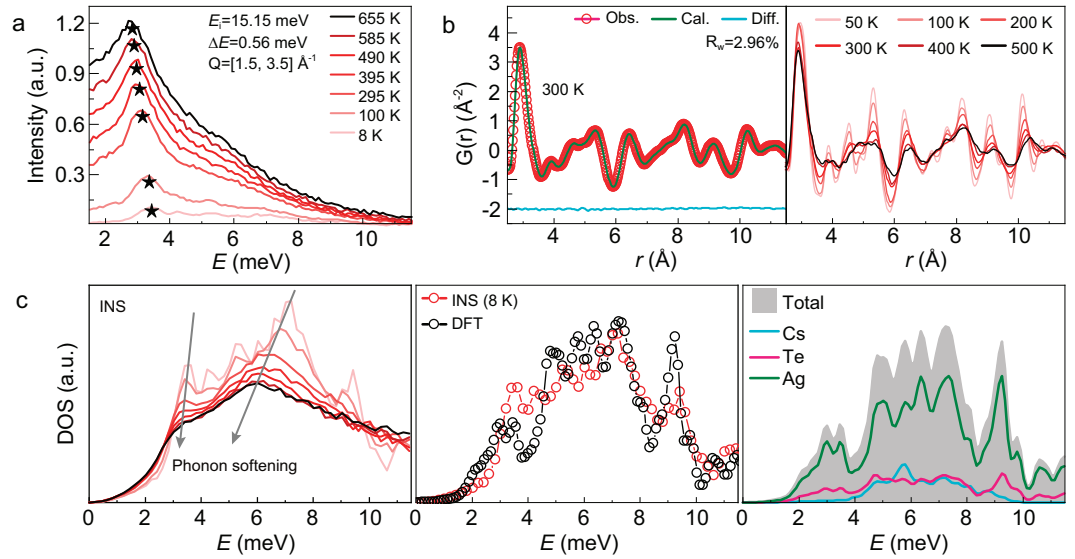
Figure 2. Temperature-dependent vibrational properties and local structures of CsAg$_5$Te$_3$. (a) The cuts of $S(\mathbf{Q}, E)$ at $E_i = 15.15$ meV integrated over the range of $1.5 \leq \mathbf{Q} \leq 3.5$ Å^{-1} under all measured temperatures. (b) Neutron PDF data at the indicated temperatures, where the room-temperature neutron PDF data are refined using the *P*4$_2$/*mnm* space group (ambient crystal structure) with all atom positions and thermal parameters refined. (c) (Left) Neutron-weighted phonon DOS from the AMATERAS measurements at the indicated temperatures with phonon softening. The DOS at lower phonon frequencies (<1 meV) are fitted to the Debye model. (Middle) Calculated generalized phonon DOS from DFT lattice dynamics and neutron-weighted phonon DOS from INS at 8 K. (Right) The partial phonon DOSs on Cs, Ag and Te from DFT.

atoms exceed or approach to the criterion of melting (≥ 0.07) as in liquids [40]. This indicates that the oscillation amplitudes of the Ag atoms are much larger than those of the Cs/Te atoms and they have liquid-like motions as a melting sublattice in the crystal with weak chemical binding. Nonetheless, the complete structural skeleton is preserved with the coexisting crystal–liquid duality [41], unlike materials with liquid-like states characterized by atomic diffusions [40].

To investigate the temperature effect on phonons, we resolve the phonon density of states (PhDOSs) from the temperature-dependent INS measurements. As shown in Fig. 2c, the PhDOS at 8 K presents several pronounced peaks at 3.5, 4.2, 5.4, 6.9 and 9.1 meV. These positions are related to the flat branches in Fig. S4. Consistently with S($\mathbf{Q}$, E) in Fig. 2a, upon heating, the peak in Fig. 2c at ∼3.5 meV is broadened and softened, while the other features eventually disappear into a broad bulge. Meanwhile, the density functional theory (DFT)-based simulations yield a total PhDOS with low-energy peaks at 3.0, 3.5, 4.9, 5.8, 6.4, 7.3 and 9.3 meV. Although there are differences in the intensity, number and position of phonons obtained from theory and experiment, the overall trend from theory is very close to that of the INS PhDOS at 8 K. In fact, we should be aware that theoretical calculations depend on the pseudopotential and some settings, while there must

be errors between experimental measurements and true values. All these factors can lead to differences between theoretical and experimental values. The partial PhDOSs can be given by:

$$g_i(\omega) = \sum_{j,\mathbf{q}} \left| e_i(j, \mathbf{q}) \right|^2 \delta(\omega - \omega(j, \mathbf{q})),$$

where ω and e_i denote the phonon energies and eigenvectors, respectively, and i is the atom index. The partial PhDOSs clearly show that the low-energy peaks ranging from 2 to 4 meV are overwhelmingly contributed by the structural tunnels dominated by the soft Ag–Te bonds [34]. The existence of soft bonds is also evaluated by elastic properties in Table S1. Importantly, this soft bonding is correlated with the strong lattice anharmonicity measured by the phonon softening with increasing temperature, as indicated in Fig. 2c.

Two-channel thermal conductivity

As discussed above, CsAg$_5$Te$_3$ has a well-ordered crystalline atomic structure, but features the liquid-like motions of Ag atoms. To accurately predict the κ_L, we solve the Wigner transport equation by simultaneously considering the particle-like and the wave-like conduction mechanisms from both the population and coherence contributions [41,42]. In
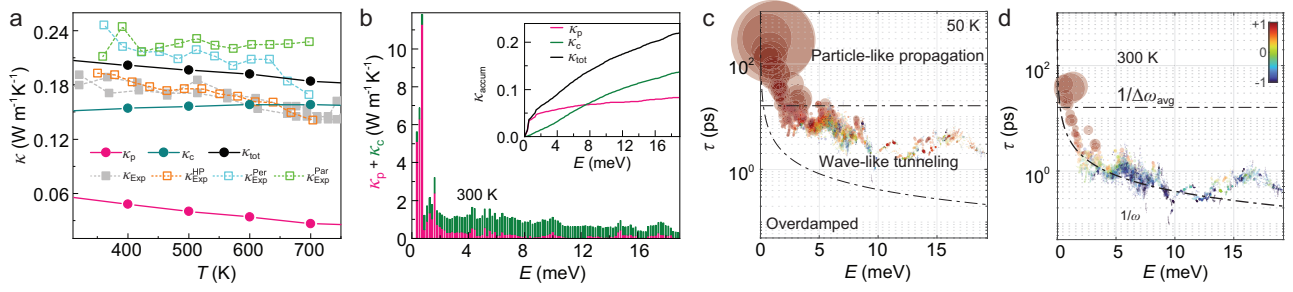
Figure 3. Thermal conductivity of CsAg$_5$Te$_3$. (a) Measured temperature-dependent lattice thermal conductivity ($\kappa_{Exp}^{HP, Per, Par}$) and the calculated values ($\kappa_{tot} = \kappa_p + \kappa_c$) from first-principles simulations, where $\kappa_{Exp}^{Per, Par}$ indicate the values parallel and perpendicular to the pressing directions with the SPS method, κ_{Exp}^{HP} represents the values of the hot-pressed sample, κ_{Exp} are values extracted from our previous work [29], κ_p and κ_c account for the heat transfer associated with the diagonal (populations) and the off-diagonal (coherences) Wigner distribution elements, respectively, and κ_{tot} is the total lattice conductivity. The results of κ_{Exp}^{Per} and κ_{Exp}^{Par} are nearly the same, indicating the good reliability of our results. (b) Phonon-mode-resolved thermal conductivities of populations (κ_p) and coherences (κ_c) at 300 K. Inset: the cumulative total thermal conductivity (κ_{tot}) as a sum of the population contribution (κ_p) and coherences contribution (κ_c) at 300 K. (c and d) Phonon lifetimes $\tau(\mathbf{q}) = [\Gamma(\mathbf{q})]^{-1}$ as a function of the energy $\omega(\mathbf{q})$ at 50 (left) and 300 K (right), respectively, where the area of each circle is proportional to the contribution to the κ_L and the colors indicate the origin of the contribution by $c = \frac{\kappa_p - \kappa_c}{\kappa_p + \kappa_c}$: $c = 1$ for particle-like propagation of the populations, $c = -1$ for wave-like tunneling of coherences and the intermediate values for phonons contributed from both mechanisms.

our transport experiment, the measured κ_L value is $\sim$0.19–0.25 W m^{-1} K^{-1}, based on subtracting κ_e in Fig. S13 from the total κ in Fig. S14. To compare experimental data with theory, the calculated κ of the sample is averaged along the three crystallographic axes. The calculated anisotropic κ is shown in Fig. S15. As shown in Fig. 3a, the calculated population contribution κ_p is equal to 0.09 W m^{-1} K^{-1} at 300 K, which is much lower than our measured values and the reported result (0.18 W m^{-1} K^{-1}) [29]. This means that, for CsAg$_5$Te$_3$, the Peierls picture breaks down in predicting κ_L when considering only the propagating vibrational waves as heat carriers. Thus, the coherence lattice thermal conductivity κ_c, from the wave-like interband (Zener) tunneling of phonons, is also considered and is calculated as 0.14 W m^{-1} K^{-1} at 300 K (see Fig. 3a). The convergent κ_L value in Fig. S16, as a sum of both κ_p and κ_c, is $\sim$0.23 W m^{-1} K^{-1} at 300 K, which coincides well with the experimental results. With increasing temperature, the κ_p decreases inversely with temperature, following the Peierls theory. This is in contrast to the observed temperature dependence of the κ_L. The contribution of the κ_c is almost unchanged and is dominant in the range of the measured temperatures. This contribution offsets the incorrect Peierls–Boltzmann conductivity and leads to our prediction of κ_L ($\kappa_L = \kappa_p + \kappa_c$) in good agreement with the experimental values. This is also consistent with the hypothesis of the well-ordered crystallized CsAg$_5$Te$_3$ containing ultralow κ_L with liquid-like vibrational properties [43,44]. Figure 3b shows the contributions of κ_p (pink) and κ_c (olive), as well as the cumulative conductivity at 300 K. The diagonal pop-

ulation contribution κ_p mainly comes from the low-lying modes of the overall crystal framework, as these modes having the largest group velocities, while all phonons that contribute to the coherence term are in a random distribution. To analyse the strength of the particle-like and the wave-like conduction, we classify the phonon lifetime $\tau(\mathbf{q})_s$ into three regimes in Fig. 3c by using the Ioffe–Regel limit ($1/\omega$) and the Wigner limit ($1/\Delta\omega_{avg}$) [41,42]. Here, the average phonon interband spacing is calculated by using $\Delta\omega_{avg} = \omega_{max}/3N_a$, where ω_{max} is the maximum phonon frequency and $3N_a$ is the number of phonon bands. These regimes operate under different mechanisms. At 50 K, as indicated in Fig. 3c, most phonons are $>1/\Delta\omega_{avg}$ and the particle-like phonons (red) propagate 87.4% of the total κ_L. In medium- and high-temperature regions, for example at 300 K as shown in Fig. 3d, the largest number of phonons are in the intermediate region between the Wigner limit and the Ioffe–Regel limit, where the heat mainly diffuses in a wave-like fashion ($\kappa_p = 0.09$ W m^{-1} K^{-1}; $\kappa_c = 0.14$ W m^{-1} K^{-1}) with the major contributors to κ_c located near the diagonal of the frequency plane between quasi-degenerate vibrational frequencies shown in Fig. S17. Note that, within the temperature range of 50–700 K, as indicated in Fig. 3 and Fig. S18, almost all phonons are above the Ioffe–Regel limit and still exhibit the well-defined quasiparticle excitations [45], despite containing the liquid-like features [43,44]. Typically, carriers exhibit wave-like behavior and diffuse via Zener-like tunneling between such quasi-degenerate vibrational eigenstates in non-crystal-like materials such as amorphous solids, glasses or liquids. Thus,

the quasiparticle excitations in $CsAg_5Te_3$, which manifest liquid-like features, give rise to the abnormal ultralow two-channel thermal conductivity.

DISCUSSION

Generally, a nonmetallic solid will always have a higher κ_L when compared with a non-convective liquid. However, the Ag and Te atoms in $CsAg_5Te_3$ have soft bonds [34]. As a result, the structural $[Ag_5Te_3]^{-1}$ tunnels undergo strong motion upon heating and the Ag atoms are almost melted in the crystal. Simultaneously, the isolated Cs^+ cations, accommodated in the tunnels, stabilize the structure and largely suppress the disorder of the Ag atoms [46]. This is very different when compared with other materials involving structural-disorder-driven liquid-like features, such as Cu_2Se [15], $AgCrSe_2$ [21] and argyrodites [25]. In these solids, the site disorder of the ions allows thermally induced ionic diffusion, which is connected to their liquid-like behavior and the reduced κ_L. In the well-ordered crystal of $CsAg_5Te_3$, although the Ag atoms exhibit large vibrational amplitudes and liquid-like motions like melting, they are still constrained and remain around their equilibrium positions due to the intrinsic structure. Instead, the special structural tunnels with soft bonds strongly scatter the phonons. The low-energy phonons range from 2 to 4 meV, are mainly contributed by the vibrations of such Ag–Te structured tunnels, exhibit large values of $\gamma_{q\nu}$ (as shown in Fig. S19) and contribute to ~70% of the total κ_p (see Fig. 3b). Meanwhile, this structure also leads to numerous low-lying optical phonons that cut the longitudinal acoustic mode, starting at ~2 meV in Fig. S4, which can be associated with the presence of the concerted rattling modes [35], as described in our previous work [29]. These traits, together with strong lattice anharmonicity ($\gamma_{tot} = 1.52$ in Fig. S19), effectively disrupt the heat propagation, which accordingly gives rise to the extremely low two-channel κ_L and almost temperature independence of the κ_L from 300 to 700 K in $CsAg_5Te_3$. The liquid-like features in this well-ordered crystal indicate a promising general strategy for obtaining high-performance energy conversion materials with ultralow κ_L. Structurally, materials with rattling-atom-based tunnels (such as Cu, Ag atoms) occupied by heavy atoms as well as having a well-ordered structure and hierarchical soft bonds [34,35,46–50] could be used to achieve ultralow thermal conduction. Differently from the general phonon–glass electron-crystal strategy that disrupts phonon transport by introducing disorder through alloying, nanostructuring and defect, our studies provide a useful way for realizing ultralow κ in materials with a low-energy strong scattering pattern from rattling modes as a signature.

CONCLUSIONS

In this study, we found that crystalline $CsAg_5Te_3$, despite lacking disorder, has a liquid-like ultralow κ_L value of ~0.18 W m^{-1} K^{-1} in the temperature range of 300–700 K. Based on experimental and theoretical evidence, we verified that there are abundant low-lying phonon modes propagated at ~3.1 meV dominated by the liquid-like motions of the Ag atoms. In the two-channel model, the coherence contributions toward the κ_L come from wavelike phonon tunneling, dominated by the process of heat transport. By solving the Wigner formulation of thermal transport, our calculated κ_L offers substantially good agreement with the measured data. Our results attest to the liquid-like heat transfer in a well-ordered crystal as a paradigm-shifting approach beyond the classic 'phonon–glass electron-crystal' paradigm in the design of low-κ_L materials. We believe that our work can significantly promote the development of thermoelectrics, thermal management, thermal barrier coatings, thermal insulators, materials science and energy conservation.

MATERIALS AND METHODS
Synthesis

All synthesizing manipulations were conducted in a glove box (moisture and oxygen levels of <0.1 ppm) or under a vacuum. Polycrystalline $CsAg_5Te_3$ samples were prepared from a mixture of Ag (shot, 99.999%, Alfa Aesar), Te (shot, 99.9999%, Alfa Aesar) and Cs_2Te_3 at a stoichiometric ratio of 10 : 3 : 1. The reactants were loaded into a fused-silica tube under a vacuum and heated to 1073 K, maintained at this temperature for 2 h and then cooled to room temperature. The obtained ingot was ground into fine powder using agate mortar to reduce the grains to <4 mm in diameter. The powdered compounds were obtained as pure phases.

Thermal conductivity

The obtained powders were then placed inside a 12.7-mm-diameter graphite die and densified by using spark plasma sintering (SPS, SPS-211LX, Fuji Electronic Industrial Co., Ltd.) at 723 K for 10 min under an axial compressive stress of 50 MPa in a vacuum. After this treatment, we obtained highly dense disk-shaped pellets, with densities of >97% of the theoretical value (7.117 g/cm^3). The pellets were

12.7 mm in diameter and 12 mm thick. Some of the obtained products were ground into fine powders that were subsequently condensed to a high density of >97% using a hot-pressed-only process at 500 K under a pressure of 60 MPa for 1 h (denoted as the hot-pressed sample). The electrical resistivity was measured in a low-pressure helium atmosphere using a ULVAC-RIKO ZEM-3 instrument system. The thermal diffusivity (D) was measured on a sample disk with a diameter of 12.7 mm and a thickness of 1.0 mm under an argon atmosphere in the range of 296–773 K by the laser flash diffusivity method using a commercial Netzsch LFA457 instrument. The heat capacity (C_p) was obtained by using a Netzsch DTA 404 PC instrument. Prior to testing, a uniform graphite layer needed to be sprayed onto the surface of the material to achieve thermal conductivity. During the testing process, the Cape Lehman+ pulse model was selected for correction. The total thermal conductivity was calculated by using the following formula:

$$\kappa = D \times C_p \times d,$$

where d is the sample density, determined by using the dimensions and mass of the sample and then re-confirmed by measurements using a gas pycnometer (Micromeritics AccuPyc 1340). According to $\kappa_e = L\sigma T = \kappa - \kappa_L$, the lattice thermal conductivity κ_L could be obtained by subtracting κ_e from κ with a Lorenz number (L) of 1.5×10^{-8} V^2 K^{-2}.

Neutron diffraction measurements

Neutron powder diffraction measurements were performed using a multi-physics instrument [51] at the China Spallation Neutron Source (CSNS) [52], in China. The data were collected at 200, 300, 400 and 500 K for the $CsAg_5Te_3$ sample. The Rietveld refinements of the neutron diffraction data at 300 K for the crystal structures of the compound were conducted using the general structure analysis system (GSAS-II) package. The real-space refinement of the experimental $G(r)$ was performed by using the PDFgui [53] program. In the refinement, the positions of all atoms in the unit cell were written and refined, and the symmetry constraints were generated by the symmetry of the space group.

INS measurements

The INS measurements were performed by using a cold neutron disc chopper spectrometer BL14 AMATERAS [54] with a beam power of ∼830 kW at the Materials and Life Science Experimental Facility (MLF), J-PARC in Japan. The chopper configurations were set with incident energies E_i of

15.15 and 41.98 meV, and corresponding energy resolutions of 0.56 and 2.44 meV (full width at the half maximum of the elastic peaks). A 5.97-g $CsAg_5Te_3$ powder sample was encased in a double cylindrical aluminum cell (14 mm in diameter, 1 mm thick) and the neutron beam size was ∼20 mm wide and ∼40 mm high. Thus, the sample was completely immersed in the neutron beam. A top-loading closed cycle refrigerator (TL-CCR) was used for the temperature-dependent measurements at 8, 100, 295, 395, 490, 585 and 655 K. The average data collection time at high temperatures was ∼3 h, which was doubled at 295 K. Data reduction was completed using the Utsusemi software suite [55]. The background, contributed by the TL-CCR with the same double cylindrical aluminum cell, was measured at the same temperatures with the same instrument configurations and was subtracted properly. The resulting dynamic structure factor $S(\mathbf{Q}, E)$ was defined as a function of the neutron energy transfer $E = E_i - E_f$ and the momentum transfer $\mathbf{Q} = \mathbf{k}_i - \mathbf{k}_f = \mathbf{q} + \boldsymbol{\tau}$, where E_f is the scattered neutron energy, $\mathbf{k}_i(\mathbf{k}_f)$ denotes the incident (scattered) neutron wave-vector, $\mathbf{q}$ is the phonon wave-vector and $\boldsymbol{\tau}$ is the reciprocal lattice vector. $S(\mathbf{Q}, E)$ was further visualized in the Mslice of the data analysis and visualization environment (DAVE) [56]. Neutron absorption correction was conducted by considering both the coherent and incoherent scattering cross sections and the absorption cross section was corrected by utilizing the Mslice/DAVE. The generalized $\mathbf{Q}$-dependent phonon density of states (GP-DOSs), $G(\mathbf{Q}, E)$, were related to the dynamic structure factor, $S(\mathbf{Q}, E)$, by the following equation [57]:

$$G(\mathbf{Q}, E) = e^{Q^2 u^2}\left[1 - e^{-\frac{E}{k_B T}}\right]\frac{E}{Q^2} S(\mathbf{Q}, E),$$

where $\left[1 - e^{-\frac{E}{k_B T}}\right]$ indicates the Bose–Einstein statistics, $e^{Q^2 u^2}$ describes the Debye–Waller factor, u is the atomic thermal displacement, k_B is the Boltzmann constant and T is the temperature. The Debye–Waller factor was ignored by setting $u = 0$ for the $\mathbf{Q}$-integrated GPDOS calculation. The impact was minimal, as we integrating a short $\mathbf{Q}$ range of 1.5–3.5 $Å^{-1}$ for $E_i = 15.15$ meV and 3.0–5.5 $Å^{-1}$ for $E_i = 41.98$ meV, with the data shown in arbitrary units.

Computational details

First-principles calculations were performed within the framework of the Perdew–Burke–Ernzerhof [58] generalized gradient approximation (PBE–GGA) [59,60], as implemented in the Vienna *ab initio* simulation package (VASP) [61]. The cut-off

energy for the plane-wave expansion was set as 500 eV on a $3 \times 3 \times 11$ Γ-centered $\mathbf{k}$-mesh. All structures were fully relaxed until the residual forces on each atom were <0.01 eV/Å and the high-symmetry lines of the tetragonal lattices were used according to previous calculations [62]. The second-order force constants were calculated within the harmonic approximation using the finite-displacement method [63] on a $5 \times 5 \times 5$ $\mathbf{k}$-mesh for $CsAg_5Te_3$, with a $1 \times 1 \times 3$ supercell (containing 108 atoms) using Phonopy code [64] bundled with VASP. The MD calculations were performed with a $1 \times 1 \times 3$ supercell via a canonical ensemble and a Nosè–Hoover thermostat. At temperatures of 200, 300, 400, 500, 600, 700 and 800 K, the MD simulations were calculated using a plane-wave cut-off of 500 eV and a total time of 50 ps, setting 1 fs as the time step. The corrections to the second-order force constants due to the finite-temperature anharmonic effects were applied using the DynaPhoPy code [65] from MD at different temperatures.

The third-order force constants were computed on a $3 \times 3 \times 3$ $\mathbf{k}$-mesh and interactions up to the third-nearest neighbors were considered, using the Phono3py [66] package. The temperature-dependent second-order force constants and third-order force constants were Fourier-interpolated on a convergent $(8 \times 8 \times 8)$ grid for thermal conductivity calculations and then generalized to an expression including both the population and coherence contributions [41,42], $\kappa_L = \kappa_p + \kappa_c$, with $\kappa_p = \frac{1}{(2\pi)^3} \int_{\mathcal{B}} \sum_s C(\boldsymbol{q})_s V^\alpha(\boldsymbol{q})_{s,s} V^\beta(\boldsymbol{q})_{s,s} \frac{1}{\Gamma(\boldsymbol{q})_s} d^3 q$ and $\kappa_c = \frac{1}{(2\pi)^3} \int_{\mathcal{B}} \sum_{s \neq s'} \frac{\omega(\boldsymbol{q})_s + \omega(\boldsymbol{q})_{s'}}{4} \left[\frac{C(\boldsymbol{q})_s}{\omega(\boldsymbol{q})_s} + \frac{C(\boldsymbol{q})_{s'}}{\omega(\boldsymbol{q})_{s'}} \right] V^\alpha(q)_{s,s'} V^\beta(q)_{s',s} \times \frac{\frac{1}{2}[\Gamma(\boldsymbol{q})_s + \Gamma(\boldsymbol{q})_{s'}]}{[\omega(\boldsymbol{q})_s - \omega(\boldsymbol{q})_{s'}]^2 + \frac{1}{4}[\Gamma(\boldsymbol{q})_s + \Gamma(\boldsymbol{q})_{s'}]^2} d^3 q$, where κ_p is the standard Peierls contribution to conductivity and the additional tensor, κ_c, is derived from the coherence equation. The κ of the polycrystalline sample was further averaged along the three principal crystallographic axes [67]. Besides, we also calculated the κ_L, κ_p and κ_c at 300 K for $CsAg_5Te_3$ with force constants being extracted by using temperature dependent effective potential technique [68,69] as contrasts in Table S2.

To compare with the experimental data from the multi-E_i time-of-flight INS, the GPDOS of $CsAg_5Te_3$ was calculated by summing the partial PhDOS values weighted by the atomic scattering cross sections and masses:

$$\text{GPDOS} = \sum_i \frac{\sigma_i}{\mu_i} \text{PhDOS}_i,$$

where σ_i and *PhDOS*$_i$ represent the atomic scattering cross section and the PhDOS projected into the individual atoms, respectively. The two-dimensional $S(\mathbf{Q}, \text{E})$ patterns, as shown in Fig. 1, were calculated from the second-order force constants with the Euphonic package [70]:

$$S(\mathbf{Q}, \text{E}) = \frac{1}{2} \sum_\nu \left| F(\mathbf{Q}, \nu) \right|^2$$
$$\times \left(n_{q\nu} + \frac{1}{2} \pm \frac{1}{2} \right) \delta \left(\omega - \mp \omega_{q\nu} \right),$$

where the upper and lower signs refer to the phonon creation and annihilation, respectively, $n_{\mathbf{q}\nu}$ is the Bose population function and $F(\mathbf{Q}, \nu)$ is the coherent one-phonon scattering structure factor.

SUPPLEMENTARY DATA

Supplementary data are available at *NSR* online.

AUTHOR CONTRIBUTIONS

B.T.W. and J.Q.H. conceived and supervised this project. P.F.L., X.Y.L., M.K., M.N., F.W.W., J.R.Z. and B.T.W. designed and performed the INS experiment using AMATERAS at J-PARC. P.F.L., J.P.X, W.Y., T.J.L. and B.T.W. designed and performed the neutron diffraction experiment using MPI at CSNS. H.L. prepared the samples and conducted the transport measurements. P.F.L., X.Y.L., L.X., J.Q.H., J.M. and B.T.W. analyzed the experimental data, along with all co-authors. P.F.L., J.Y.L., J.B.Z., Z.T., Y.S.Z. and B.T.W. performed the ab initio calculations and analyzed the data. P.F.L. X.Y.L., D.J.S., H.L., J.R.Z., J.Q.H. and B.T.W. drafted the manuscript. All authors analyzed and reviewed the results, and provided input for the manuscript.

Conflict of interest statement. None declared.

REFERENCES

1. Sun WJ. Scalable thermal insulator. *Nat Nanotechnol* 2018; **13**: 272.

2. Vagge ST and Ghogare S. Thermal barrier coatings: review. *Materials Today-Proceedings* 2022; **56**: 1201–16.

3. Yan QY and Kanatzidis MG. High-performance thermoelectrics and challenges for practical devices. *Nat Mater* 2022; **21**: 503–13.

4. Kozinsky B and Singh DJ. Thermoelectrics by computational design: progress and opportunities. *Annu Rev Mater* 2021; **51**: 565–90.

5. Chen ZW, Zhang XY, Pei YZ. Manipulation of phonon transport in thermoelectrics. *Adv Mater* 2018; **30**: 1705617.

6. Roychowdhury S, Ghosh T, Arora R *et al.* Enhanced atomic ordering leads to high thermoelectric performance in AgSbTe. *Science* 2021; **371**: 722–7.

7. Jiang BB, Yu Y, Cui J *et al.* High-entropy-stabilized chalcogenides with high thermoelectric performance. *Science* 2021; **371**: 830–4.

8. Qin BC, Wang DY, Zhao LD. Slowing down the heat in thermoelectrics. *Infomat* 2021; **3**: 755–89.

9. Li CW, Hong J, May AF *et al.* Orbitally driven giant phonon anharmonicity in SnSe. *Nat Phys* 2015; **11**: 1063–9.

10. Jana MK and Biswas K. Crystalline solids with intrinsically low lattice thermal conductivity for thermoelectric energy conversion. *Acs Energy Letters* 2018; **3**: 1315–24.

11. Delaire O, Ma J, Marty K *et al.* Giant anharmonic phonon scattering in PbTe. *Nat Mater* 2011; **10**: 614–9.

12. Carruthers P. Theory of thermal conductivity of solids at low temperatures. *Rev Mod Phys* 1961; **33**: 92–138.

13. Takabatake T, Suekuni K, Nakayama T. Phonon-glass electron-crystal thermoelectric clathrates: experiments and theory. *Rev Mod Phys* 2014; **86**: 669–716.

14. Trachenko K and Brazhkin VV. Collective modes and thermodynamics of the liquid state. *Rep Prog Phys* 2016; **79**: 016502.

15. Liu HL, Shi X, Xu FF *et al.* Copper ion liquid-like thermoelectrics. *Nat Mater* 2012; **11**: 422–5.

16. Voneshen DJ, Walker HC, Refson K *et al.* Hopping time scales and the phonon-liquid electron-crystal picture in thermoelectric copper selenide. *Phys Rev Lett* 2017; **118**: 145901.

17. Niedziela JL, Bansal D, May AF *et al.* Selective breakdown of phonon quasiparticles across superionic transition in CuCrSe. *Nat Phys* 2019; **15**: 73–8.

18. Zhao KP, Qiu PF, Shi X *et al.* Recent advances in liquid-like thermoelectric materials. *Adv Funct Mater* 2020; **30**: 1903867.

19. Zhang ZX, Zhao KP, Wei TR *et al.* Cu$_2$Se-based liquid-like thermoelectric materials: looking back and stepping forward. *Energy Environ Sci* 2020; **13**: 3307–29.

20. Li LS, Liu HL, Avdeev M *et al.* Neutron scattering studies on ionic diffusion behaviors of superionic α-Cu$_{2-\delta}$Se. *Appl Phys Lett* 2022; **121**: 151901.

21. Li B, Wang H, Kawakita Y *et al.* Liquid-like thermal conduction in intercalated layered crystalline solids. *Nat Mater* 2018; **17**: 226–30.

22. Koley B, Lakshan A, Raghuvanshi PR *et al.* Ultralow lattice thermal conductivity at room temperature in Cu$_4$TiSe$_4$. *Angew Chem Int Ed* 2021; **60**: 9106–13.

23. Gupta MK, Ding JX, Bansal D *et al.* Strongly anharmonic phonons and their role in superionic diffusion and ultralow thermal conductivity of Cu$_7$PSe$_6$. *Adv Energy Mater* 2022; **12**: 2200596.

24. Ren QY, Gupta MK, Jin M *et al.* Extreme phonon anharmonicity underpins superionic diffusion and ultralow thermal conductivity in argyrodite Ag$_8$SnSe$_6$. *Nat Mater* 2023; **22**: 999–1006.

25. Lin SQ, Li W, Pei YZ. Thermally insulative thermoelectric argyrodites. *Mater Today* 2021; **48**: 198–213.

26. Liu JY, Chen L, Wu LM. AgGaSe: high-pressure-induced Ag migration causes thermoelectric performance irreproducibility and elimination of such instability. *Nat Commun* 2022; **13**: 2966.

27. Dutta M, Sarkar D, Biswas K. Intrinsically ultralow thermal conductive inorganic solids for high thermoelectric performance. *Chem Commun* 2021; **57**: 4751–67.

28. Li J, Guo HY, Zhang X *et al.* CsAg$_5$Te$_3$: a new metal-rich telluride with a unique tunnel structure. *J Alloys Compd* 1995; **218**: 1–4.

29. Lin H, Tan GJ, Shen JN *et al.* Concerted rattling in CsAg$_5$Te$_3$ leading to ultralow thermal conductivity and high thermoelectric performance. *Angew Chem Int Ed* 2016; **55**: 11431–6.

30. Tee SY, Ponsford D, Lay CL *et al.* Thermoelectric silver-based chalcogenides. *Adv Sci* 2022; **9**: 204624.

31. Toberer ES, Baranowski LL, Dames C. Advances in thermal conductivity. *Annu Rev Mater* 2012; **42**: 179–209.

32. Isaeva L, Barbalinardo G, Donadio D *et al.* Modeling heat transport in crystals and glasses from a unified lattice-dynamical approach. *Nat Commun* 2019; **10**: 3853.

33. Chen J, He J, Pan DK *et al.* Emerging theory and phenomena in thermal conduction: a selective review. *Sci China-Phys Mech Astron* 2022; **65**: 117002..

34. Ma N, Li YY, Chen L *et al.* α-CsCuSe: discovery of a low-cost bulk selenide with high thermoelectric performance. *J Am Chem Soc* 2020; **142**: 5293–303.

35. Voneshen DJ, Refson K, Borissenko E *et al.* Suppression of thermal conductivity by rattling modes in thermoelectric sodium cobaltate. *Nat Mater* 2013; **12**: 1028–32.

36. Budai JD, Hong JW, Manley ME *et al.* Metallization of vanadium dioxide driven by large phonon entropy. *Nature* 2014; **515**: 535–9.

37. Pailhès S, Euchner H, Giordano VM *et al.* Localization of propagative phonons in a perfectly crystalline solid. *Phys Rev Lett* 2014; **113**: 025506.

38. Ni YX and Volz S. Evidence of phonon Anderson localization on the thermal properties of disordered atomic systems. *J Appl Phys* 2021; **130**: 190901.

39. Li XY, Liu PF, Zhao EY *et al.* Ultralow thermal conductivity from transverse acoustic phonon suppression in distorted crystalline α-MgAgSb. *Nat Commun* 2020; **11**: 942.

40. Qiu WJ, Xi LL, Wei P *et al.* Part-crystalline part-liquid state and rattling-like thermal damping in materials with chemical-bond hierarchy. *Proc Nat Acad Sci USA* 2014; **111**: 15031–5.

41. Simoncelli M, Marzari N, Mauri F. Unified theory of thermal transport in crystals and glasses. *Nat Phys* 2019; **15**: 809–13.

42. Simoncelli M, Marzari N, Mauri F. Wigner formulation of thermal transport in solids. *Phys Rev X* 2022; **12**: 041011.

43. Hosokawa S, Inui M, Kajihara Y *et al.* Transverse acoustic excitations in liquid Ga. *Phys Rev Lett* 2009; **102**: 105502.

44. Scopigno T, Ruocco G, Sette F. Microscopic dynamics in liquid metals: the experimental point of view. *Rev Mod Phys* 2005; **77**: 881–933.

45. Wang XP, Zheng W, Wang LJ *et al.* Disordered solids without well-defined transverse phonons: the nature of hard-sphere glasses. *Phys Rev Lett* 2015; **114**: 035502.

46. Ma N, Li F, Li JG *et al.* Mixed-valence CsCu$_4$Se$_3$: large phonon anharmonicity driven by the hierarchy of the rigid [(Cu$^+$)$_4$(Se^{2-})$_2$](Se$^-$) double anti-CaF$_2$ layer and the soft Cs$^+$ sublattice. *J Am Chem Soc* 2021; **143**: 18490–501.

47. Eanes ME, Schimek GL, Kolis JW. Synthesis and structural characterization of CsAg$_5$Se$_3$ and RbAg$_5$Te$_3$. *J Chem Crystallogr* 2000; **30**: 223–6.

48. Jong UG, Kang CJ, Kim SY *et al.* Superior thermoelectric properties of ternary chalcogenides CsAg$_5$Q$_3$ (Q = Te, Se) predicted using first-principles calculations. *Phys Chem Chem Phys* 2022; **24**: 5729–37.

49. He JG, Xia Y, Lin WW *et al.* Accelerated discovery and design of ultralow lattice thermal conductivity materials using chemical bonding principles. *Adv Funct Mater* 2022; **32**: 2108532.

50. Li JY, Li XY, Zhang YS *et al.* Crystal-liquid duality driven ultralow two-channel thermal conductivity in α-MgAgSb. *Appl Phys Rev* 2024; **11**: 011406.

51. Xu JP, Xia YG, Li ZD *et al.* Multi-physics instrument: total scattering neutron time-of-flight diffractometer at China Spallation Neutron Source. *Nucl Instrum Meth A* 2021; **1013**: 165642.

52. Wei J, Chen HS, Chen YW *et al.* China Spallation Neutron Source: design, R&D, and outlook. *Nucl Instrum Meth A* 2009; **600**: 10–3.

53. Farrow CL, Juhas P, Liu JW *et al.* PDFfit2 and PDFgui: computer programs for studying nanostructure in crystals. *J Phys: Condens Matter* 2007; **19**: 335219.

54. Nakajima K, Ohira-Kawamura S, Ktxucm T *et al.* AMATERAS : a cold-neutron disk chopper spectrometer. *J Phys Soc Jpn* 2011; **80**: SB028.

55. Inamura Y, Nakatani T, Suzuki J *et al.* Development status of software 'Utsusemi' for Chopper spectrometers at MLF, J-PARC. *J Phys Soc Jpn* 2013; **82**: SA031.

56. Azuah RT, Kneller LR, Qiu YM *et al.* DAVE: a comprehensive software suite for the reduction, visualization, and analysis of low energy neutron spectroscopic data. *J Res Nat Inst Stand Technol* 2009; **114**: 341–58.

57. Carpenter JM and Price DL. Correlated motions in glasses studied by coherent inelastic neutron-scattering. *Phys Rev Lett* 1985; **54**: 441–3.

58. Kresse G and Joubert D. From ultrasoft pseudopotentials to the projector augmented-wave method. *Phys Rev B* 1999; **59**: 1758–75.

59. Blochl PE. Projector augmented-wave method. *Phys Rev B* 1994; **50**: 17953–79.

60. Blochl PE, Jepsen O, Andersen OK. Improved tetrahedron method for Brillouin-Zone integrations. *Phys Rev B* 1994; **49**: 16223–33.

61. Kresse G and Furthmuller J. Efficient iterative schemes for ab initio total-energy calculations using a plane-wave basis set. *Phys Rev B* 1996; **54**: 11169–86.

62. Setyawan W and Curtarolo S. High-throughput electronic band structure calculations: challenges and tools. *Comput Mater Sci* 2010; **49**: 299–312.

63. Baroni S, de Gironcoli S, Dal Corso A *et al.* Phonons and related crystal properties from density-functional perturbation theory. *Rev Mod Phys* 2001; **73**: 515–62.

64. Togo A, Oba F, Tanaka I. First-principles calculations of the ferroelastic transition between rutile-type and $CaCl_2$-type SiO_2 at high pressures. *Phys Rev B* 2008; **78**: 134106.

65. Carreras A, Togo A, Tanaka I. DynaPhoPy: a code for extracting phonon quasiparticles from molecular dynamics simulations. *Comput Phys Commun* 2017; **221**: 221–34.

66. Togo A, Chaput L, Tanaka I. Distributions of phonon lifetimes in Brillouin zones. *Phys Rev B* 2015; **91**: 094306.

67. Tong Z, Pecchia A, Yam C *et al.* Glass-like transport dominates ultralow lattice thermal conductivity in modular crystalline $Bi_4O_4SeCl_2$. *Nano Lett* 2023; **23**: 9468–73.

68. Hellman O, Steneteg P, Abrikosov IA *et al.* Temperature dependent effective potential method for accurate free energy calculations of solids. *Phys Rev B* 2013; **87**: 104111.

69. Hellman O and Abrikosov IA. Temperature-dependent effective third-order interatomic force constants from first principles. *Phys Rev B* 2013; **88**: 144301.

70. Fair R, Jackson A, Voneshen D *et al.* Euphonic: inelastic neutron scattering simulations from force constants and visualization tools for phonon properties. *J Appl Crystallogr* 2022; **55**: 1689–703.